Mean-field effects on collective flow in high-energy heavy-ion collisions at 2–158*A* GeV energies

M. Isse* and A. Ohnishi
Division of Physics, Graduate School of Science, Hokkaido University, Sapporo, Hokkaido 060-0810, Japan

N. Otuka
Nuclear Data Center, Department of Nuclear Energy System, Japan Atomic Energy Research Institute, Tokai, Ibaraki 319-1195, Japan

P. K. Sahu
Institute of Physics, Sachivalaya Marg, Bhubaneswar 751 005, India

Y. Nara
Institut für Theoretische Physik, Johann Wolfgang Goethe-Universität, Max-von-Laue-Straße 1, D-60438 Frankfurt am Main, Germany
(Received 13 March 2005; published 29 December 2005)

Collective flows in heavy-ion collisions from AGS [(2–11)*A* GeV] to SPS [(40, 158)*A* GeV] energies are investigated in a nonequilibrium transport model with the nuclear mean field (MF). Sideward $\langle p_x \rangle$, directed v_1, and elliptic flows v_2 are systematically studied with different assumptions for the nuclear equation of state (EOS). We find that the momentum dependence on the nuclear MF is important for the understanding of the proton collective flows at AGS and SPS energies. Calculated results with momentum-dependent MF qualitatively reproduce the experimental data of proton sideward, directed, and elliptic flows in a incident energy range of (2–158)*A* GeV.

DOI: 10.1103/PhysRevC.72.064908 PACS number(s): 25.75.Ld, 24.10.−i

I. INTRODUCTION

Determining the nuclear equation of state (EOS) under various conditions has been one of the principle goals of heavy-ion physics in these decades [1–34]. Near the saturation density, the EOS gives the bulk properties of nuclei such as the binding energy and the radius. While the first-principle simulations of lattice QCD are possible for hot baryon-free nuclear matter, and while matter at low baryon densities can be studied by expanding in the power series of the baryon chemical potential μ [35], the properties of highly compressed matter are still under debate. Thus phenomenological studies are necessary to connect the experimental heavy-ion collision data with the EOS, especially for nuclear matter at high baryon densities. In high-energy heavy-ion collisions, where nuclear matter over a wide range of temperatures and densities is probed, many ideas on the EOS and phases have been examined. For example, very dense matter was created in recent RHIC experiments [36], suggesting the creation of a gas of deconfined quarks and gluons (QGP). In the 1970's and 1980's the existence of strong collective flow in heavy-ion collisions was suggested in hydrodynamics [1–3], and it was examined in experiments at Bevalac [4]. Since collective sideward flows are generated in the early stages of collisions by the repulsive nucleon potential in nuclear matter, the observed strong collective flows were believed to signal very large pressure at high baryon densities, i.e., the hard EOS [5]. On the other hand, the real part of the nucleon-nucleus potential is already repulsive at normal density at high incident energies, and the role of the momentum dependence of the nuclear potential in the collective flows was extensively studied after 1990 [5–9]. To distinguish the momentum and the density dependences, we need to invoke heavy-ion collision data over a wide incident energy range. We now have systematic collective flow data at various incident energies from the LBNL Bevalac [10–12], GSI Schwerionen Synchrotron (SIS) [13–15], MSU NSCL [16], BNL Alternating Gradient Synchrotron (AGS) [17–21], CERN Super Proton Synchrotron (SPS) [22–24], and BNL RHIC [37].

Collective flow data obtained at AGS energies [(2–11)*A* GeV] provide a good landmark to determine the EOS. As demonstrated in Ref. [25], the saturating momentum dependence of the mean-field (MF), a large number of hadronic resonances, and string degrees of freedom are essential in order to explain all of the radial, sideward, and elliptic flows at AGS energies. The momentum dependence of nuclear potentials in the context of collective flow was also discussed in Ref. [9] with a quantum molecular dynamics (QMD) model. It is suggested that we can separate the momentum dependence by analyzing the so-called balance energy at which the flow disappears, and this was later confirmed by experiment at NSCL [16] for $E_{\rm inc} = (55–155)A$ MeV. Recently, Danielewicz and others discussed the EOS with these data within a Boltzmann equation simulation [17,26–28], showing that a reliable stiffness value (K = 167–380 MeV) cannot be uniquely determined from currently available collective flow data (F or v_2) up to AGS energies [$E_{\rm inc}$ = (0.15–11)*A* GeV] [28]. On the other hand, a description comparable with theirs was also obtained in the relativistic Boltzmann-Uehling-Uhlenbeck (RBUU) model [25] by using a relativistic mean field. In RBUU, the MF is fitted to reproduce the real part of the global optical potential in Dirac phenomenology [38]. In

*Electronic address: isse@nucl.sci.hokudai.ac.jp

Ref. [25] a common MF giving $K \sim 300$ MeV is applied in the energy range of (0.25–11)A GeV. Thus these two studies do not necessarily provide the same conclusion for the stiffness. In addition, we still have large ambiguities in the MF for hadrons other than nucleons. In order to reduce these ambiguities and to pin down the EOS more precisely, recently measured flow data at lower SPS energies [(20–80)A GeV] may be helpful, because a higher baryon density would be reached at these incident energies.

Several hadronic transport models, such as RQMD [39–43], BEM [26–28], RBUU [25,32,33], ARC [44], ART [45], HSD [46], UrQMD [47,48], and JAM [49], have been successfully applied to describe many aspects of high-energy heavy-ion collisions over a wide range of incident energies. Transport models without MF effects (ARC, HSD, JAM) can describe bulk observables such as transverse mass spectra or rapidity distributions, but they cannot explain anisotropic collective flows, which are sensitive to MF potentials. Transport models with MF effects (RQMD, BEM, RBUU, ART, UrQMD) have been successful in explaining anisotropic collective flows in addition to bulk observables up to AGS energies. For SPS energies, however, the MF effects on collective flows have not been seriously investigated.

In this work, we investigate collective flows from 2A GeV to 158A GeV by using a hadronic cascade model, the jet AA microscopic transportation model (JAM) [49], combined with a covariant prescription of the MF (RQMD/S) [43].

This paper is organized as follows. In Sec. II we explain our transport model and the parametrization of our EOS used there. In Sec. III we present our results for flows on rapidity and transverse distributions as well as their excitation functions. In Sec. IV we discuss some uncertainties in our model. In Sec. V we summarize our work.

II. NONEQUILIBRIUM TRANSPORT MODEL AND THE EQUATIONS OF STATE

Heavy-ion collision is a dynamical process of a system in which the temperature and density are not uniform and the equilibrium is not necessarily reached. Therefore we need dynamical models to describe collisions in order to extract static properties of nuclear matter under equilibrium. A hydrodynamic description is the most direct way to connect the EOS and dynamics. Actually, ideal hydrodynamics has succeeded in describing elliptic flow at low p_T, up to semicentral and around mid-rapidity at RHIC [50] (however, see Ref. [51] for a recent reinterpretation of the RHIC data), where the number of produced particles is so large that local equilibrium may be easily achieved. However the condition of local equilibrium may not be satisfied up to SPS energies, and nonequilibrium dynamics is required for studying the EOS of dense nuclear matter through heavy-ion collisions.

Hadron-string cascade processes are the main source of thermalization and particle production up to SPS energies. In the increase of incident energy from AGS [(2–11)A GeV] to SPS [(20–158)A GeV], the main particle production mechanism in hadron-hadron collisions evolves from resonance productions to string formations. At higher energies, hard partonic interaction (jet production) becomes more important, and the jet production cross section reaches around 20% of the total cross section of pp at RHIC [52].

JAM includes all of the above particle and jet production mechanisms, and the applicable incident energy range is expected to be adequate (for the study of collective flow, jet production does not matter). Inelastic hadron-hadron collisions produce resonances at low energies. We explicitly include all established hadronic states with masses up to around 2 GeV with explicit isospin states as well as their antiparticles, which are made to propagate in space-time. At higher energies ($\sqrt{s} \gtrsim 4$ GeV in BB collisions, $\sqrt{s} \gtrsim 3$ GeV in MB collisions, and $\sqrt{s} \gtrsim 2$ GeV in MM collisions) color strings are formed, and they decay into hadrons after their formation time ($\tau \sim 1$ fm/c) according to the Lund string model PYTHIA [53]. Leading hadrons having constituent quarks can scatter within their formation time with other hadrons, assuming the additive quark cross section that is known to be important at SPS energies [48].

It is necessary to include MF effects to explain collective flow data, and the MF should have momentum dependence as well as density dependence in order to describe flows over a wide incident energy range. We adopt here a simple Skyrme-type density-dependent MF in the zero-range approximation and a Lorentzian-type momentum-dependent MF [6] that simulates the exchange term (Fock term) of the Yukawa potential. The single-particle potential U then has the form

$$U(\boldsymbol{r}, \boldsymbol{p}) = \alpha \left(\frac{\rho(\boldsymbol{r})}{\rho_0}\right) + \beta \left(\frac{\rho(\boldsymbol{r})}{\rho_0}\right)^{\gamma} + \sum_{k=1,2} \frac{C_{\rm ex}^{(k)}}{\rho_0} \int d\boldsymbol{p}' \frac{f(\boldsymbol{r}, \boldsymbol{p}')}{1 + [(\boldsymbol{p} - \boldsymbol{p}')/\mu_k]^2}. \quad (1)$$

This MF potential leads to the following total potential energy, through the relation $U = \delta V/\delta f$:

$$V = \int d\boldsymbol{r} \left[\frac{\alpha \rho^2(\boldsymbol{r})}{2\rho_0} + \frac{\beta \rho^{\gamma+1}(\boldsymbol{r})}{(1+\gamma)\rho_0^{\gamma}}\right] + \sum_{k=1,2} \frac{C_{\rm ex}^{(k)}}{2\rho_0} \int d\boldsymbol{r}\, d\boldsymbol{p}\, d\boldsymbol{p}' \frac{f(\boldsymbol{r}, \boldsymbol{p}) f(\boldsymbol{r}, \boldsymbol{p}')}{1 + [(\boldsymbol{p} - \boldsymbol{p}')/\mu_k]^2}, \quad (2)$$

where $f(\boldsymbol{r}, \boldsymbol{p})$ is the phase space distribution function whose integral over $\boldsymbol{p}$ is normalized to the density $\rho(\boldsymbol{r})$. At zero temperature the phase space distribution function is given as

$$f(\boldsymbol{r}, \boldsymbol{p}) = \left(\frac{4}{3}\pi p_F^3\right)^{-1} \rho(\boldsymbol{r})\, \Theta(p_F - |\boldsymbol{p}|). \quad (3)$$

Then the total energy per nucleon is

$$\frac{E}{A}(\rho) = \frac{3}{5}\frac{p_F(\rho)^2}{2m} + \frac{\alpha}{2\rho_0}\rho + \frac{\beta}{(1+\gamma)\rho_0^{\gamma}}\rho^{\gamma} + \frac{\rho}{2\rho_0}\left(\frac{4}{3}\pi p_F^3\right)^{-2} \times \int_0^{p_F} d\boldsymbol{p} \int_0^{p_F} d\boldsymbol{p}' \sum_{k=1,2} \frac{C_{\rm ex}^{(k)}}{1 + [(\boldsymbol{p} - \boldsymbol{p}')/\mu_k]^2}, \quad (4)$$

TABLE I. Parameter set of density-dependent and momentum-dependent/independent potentials. Momentum-dependent hard (MH) and soft (MS) potentials are taken from Ref. [55] with simplification (see text for detail). Momentum-independent hard (H) and soft (S) potentials are taken from Ref. [56].

Type	α (MeV)	β (MeV)	γ	$C_{\rm ex}^{(1)}$ (MeV)	$C_{\rm ex}^{(2)}$ (MeV)	μ_1 (fm^{-1})	μ_2 (fm^{-1})	K (MeV)
MH	−33	110	5/3	−277	663	2.35	0.4	448
MS	−268	345	7/6	−277	663	2.35	0.4	314
H	−124	70.5	2	—	—	—	—	380
S	−356	303	7/6	—	—	—	—	200

where the Fermi momentum is taken to be $p_F(\rho) = \hbar(3\pi^2\rho/2)^{1/3}$. See Eq. (A22) for the definition of ρ used in the actual simulations. Integrals in Eq. (4) can be obtained analytically [7] as

$$\int_0^{p_F} d\boldsymbol{p} \int_0^{p_F} d\boldsymbol{p}' \frac{1}{1+[(\boldsymbol{p}-\boldsymbol{p}')/\mu]^2} = \frac{32\pi^2}{3} p_F^4 \mu^2 \left\{ \frac{3}{8} - \frac{\mu}{2p_F} \arctan\frac{2p_F}{\mu} - \frac{\mu^2}{16p_F^2} + \left[\frac{3}{16}\frac{\mu^2}{p_F^2} + \frac{1}{64}\frac{\mu^4}{p_F^4} \ln\left(1+\frac{4p_F^2}{\mu^2}\right)\right]\right\}. \quad (5)$$

Parameters α, β, and γ in Eq. (4) are determined to reproduce the saturation of the total energy per nucleon at the normal nuclear density, i.e., $E/A|_{\rho=\rho_0} = -16$ MeV and $P = \rho^2\partial(E/A)/\partial\rho|_{\rho=\rho_0} = 0\,\mathrm{MeV/fm^3}$ [54]. The incompressibility K is obtained from $K = 9\rho^2\partial^2(E/A)/\partial\rho^2|_{\rho=\rho_0}$. Parameters for the hard (H) and soft (S) EOS are listed in Table I, and the density dependences of the total energy per nucleon are shown in the right-hand panel of Fig. 1.

Parameters $C_{\rm ex}^{(k)}$ and μ_k are taken to reproduce the real part of the global Dirac optical potential (Schrödinger equivalent potential) of Hama *et al*. [38], in which angular distribution and polarization quantities in proton-nucleus elastic scatterings are analyzed in the range of 10 MeV to 1 GeV in Dirac phenomenology. The single-particle potential at $\rho = \rho_0$,

$$\begin{aligned} U(\boldsymbol{p},\rho_0) &= \alpha+\beta+\left(\frac{4}{3}\pi p_F^3\right)^{-1} \times \int_0^{p_F} d\boldsymbol{p}' \sum_{k=1,2} \frac{C_{\rm ex}^{(k)}}{1+[(\boldsymbol{p}-\boldsymbol{p}')/\mu_k]^2} \\ &= \alpha+\beta+\left(\frac{4}{3}\pi p_F^3\right)^{-1} \times \sum_{k=1,2} C_{\rm ex}^{(k)} \pi\mu_k^3 \left[\frac{p_F^2+\mu_k^2-p^2}{2p\mu_k} \ln\frac{(p+p_F)^2+\mu_k}{(p-p_F)^2+\mu_k} + \frac{2p_F}{\mu_k} - 2\left(\arctan\frac{p+p_F}{\mu_k} - \arctan\frac{p-p_F}{\mu_k}\right)\right], \end{aligned} \quad (6)$$

is compared with the Schrödinger equivalent potential from Ref. [38] in the left-hand panel of Fig. 1. Parameters for the momentum-dependent potentials are shown as MH and MS in Table I. These parameter sets are based on Ref. [55] with a simplification in which the Coulomb, surface, and Pauli potentials as well as the zero-point kinetic energy of the Gaussian wave packets are dropped, because their study focused on nuclear matter below the saturation density. We have fixed the high-energy limit of the optical potential $U \to 77$ MeV at $E_{\rm inc} \to \infty$, leading to a constraint $\alpha+\beta = 77$ MeV. This constraint generally makes the EOS stiffer than those in Ref. [31].

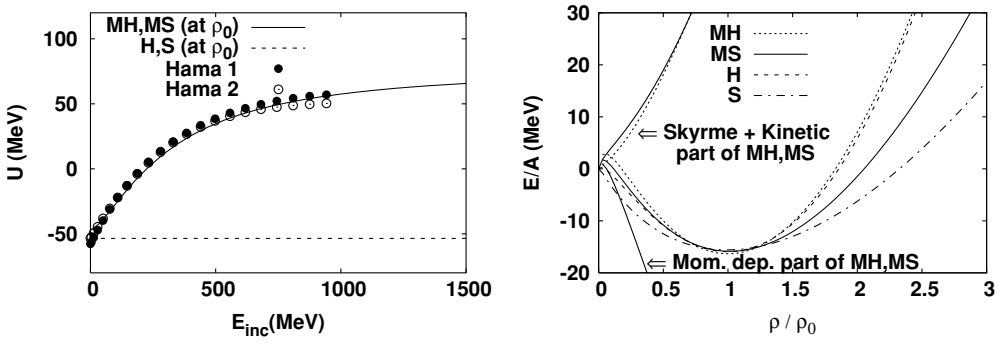

FIG. 1. Left, momentum dependence of the single-particle potentials, Eq. (6), for momentum-dependent hard (MH) and soft (MS) and momentum-independent hard (H) and soft (S) potentials are compared with the real part of the global Dirac optical potential [38]. Right, density dependence of total energy per nucleon in Eq. (4) for momentum-dependent (MH, MS) and -independent (H, S) potentials.

We include the above MF effects in JAM [49] by means of simplified RQMD (RQMD/S) [43] framework. The relativistic quantum molecular dynamics (RQMD) model [39,40,42] is a constrained Hamiltonian dynamics, in which potentials are treated in a covariant way. RQMD/S [43] uses much simpler and more practical time fixation constraints than the original RQMD [39,40,42]. For details, see Appendix.

In this work we take into account potential interactions only between baryons. The simulation time step size is taken to be $dt = 0.1$ fm/c at all incident energies. We discuss the influence of MF for nonnucleonic baryons on the flow analysis and the validity of this treatment in Sec. IV. The magnitude of the energy conservation violated is about 0.4% on average for time and events.

III. COLLECTIVE FLOWS FROM AGS TO SPS ENERGIES

When two heavy nuclei collide at high energies at finite impact parameters, the pressure gradient is anisotropic in the initial stages of the collision. As a result, it generates anisotropic collective flows. Until now, several kinds of collective flows have been proposed for probing highly dense matter. The first is the sideward flow (also called directed flow) $\langle p_x \rangle$, which is defined as the mean value of p_x, where x is defined as the impact parameter direction on the reaction plane. Sideward flow is generated mainly by the participant-spectator interaction. Nucleons in the projectile feel repulsive interaction from the target nucleus during the projectile-target contact time. This repulsion pushes projectile nucleons out in the positive sideward direction if the contact time is long enough. When the incident energy is very high, the contact time in collisions becomes shorter owing to the Lorentz contraction; therefore sideward flow decreases. At SPS energies mainly other types of collective flows, called directed (v_1) and elliptic (v_2) flows, are measured. These are defined as the nth Fourier coefficient,

$$\frac{d^3N}{p_T dp_T dy d\phi} = \frac{d^2N}{2\pi p_T dp_T dy}\left(1 + \sum_n 2v_n(p_T, y)\cos n\phi\right), \tag{7}$$

where the azimuthal angle ϕ is measured from the reaction plane. The directed flow v_1 is the first Fourier coefficient of the azimuthal distribution

$$v_1 = \langle \cos\phi \rangle = \left\langle \frac{p_x}{p_T} \right\rangle, \tag{8}$$

and the elliptic flow v_2 is the second Fourier coefficient of the azimuthal distribution

$$v_2 = \langle \cos 2\phi \rangle = \left\langle \frac{p_x^2 - p_y^2}{p_T^2} \right\rangle. \tag{9}$$

These collective flows are reviewed in Ref. [57].

The effects of the MF in high-energy heavy-ion collisions are visible but not very large in single-particle spectra, such as the rapidity distribution dN/dy or the transverse mass distribution $d^2N/m_T dm_T dy$. In this section we demonstrate that MF effects are essential for studying anisotropic collective flows in the hadron-string transport model JAM with MF potentials.

A. Collective flows at AGS energies

We show proton sideward flow $\langle p_x \rangle$ in mid-central Au+Au collisions at AGS energies [$E_{\rm inc} = (2\text{–}11)A$ GeV] together with AGS-E895 data [20] in Fig. 2 and in the left-hand panel of Fig. 3. We choose the impact parameter range $4 < b < 8$ fm in the calculations, which roughly corresponds to mid-central collisions in experimental data.

It is seen that both cascade and momentum-independent soft (S) MF results are inconsistent with the data. The magnitude

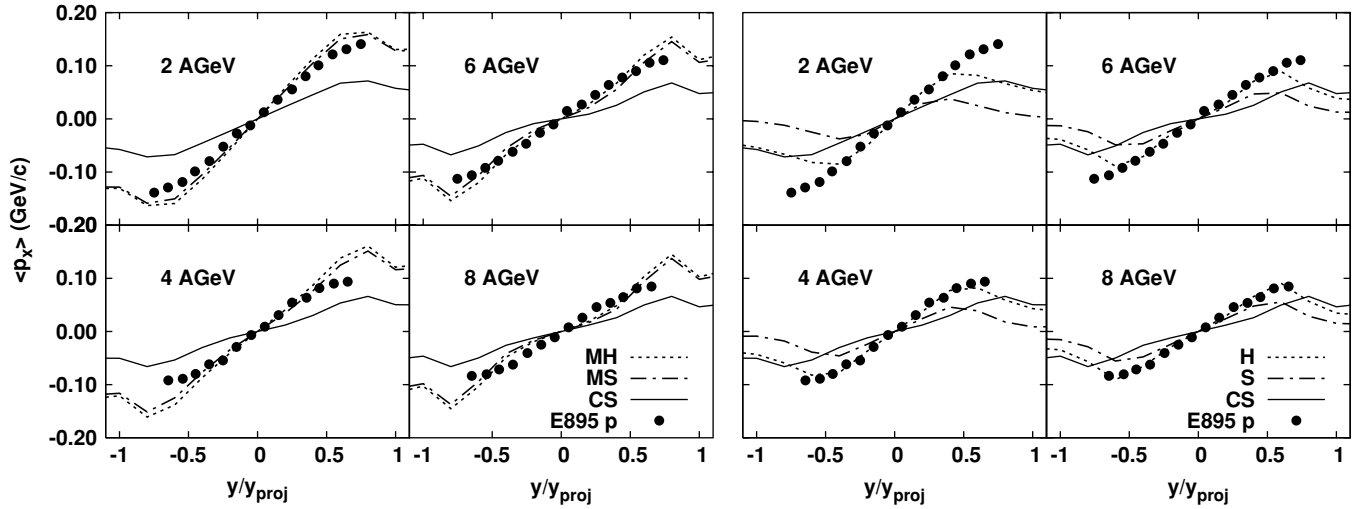

FIG. 2. Sideward flows $\langle p_x \rangle$ of protons in mid-central Au+Au collisions at (2–8)A GeV are compared with the AGS-E895 data [20]. Curves show the calculated results of cascade with momentum-dependent hard or soft mean field (MH or MS, left-hand panels), cascade with momentum-independent mean field (H or S, right-hand panels), and cascade without mean field (CS). The experimental data are shown in both the left and the right panels.

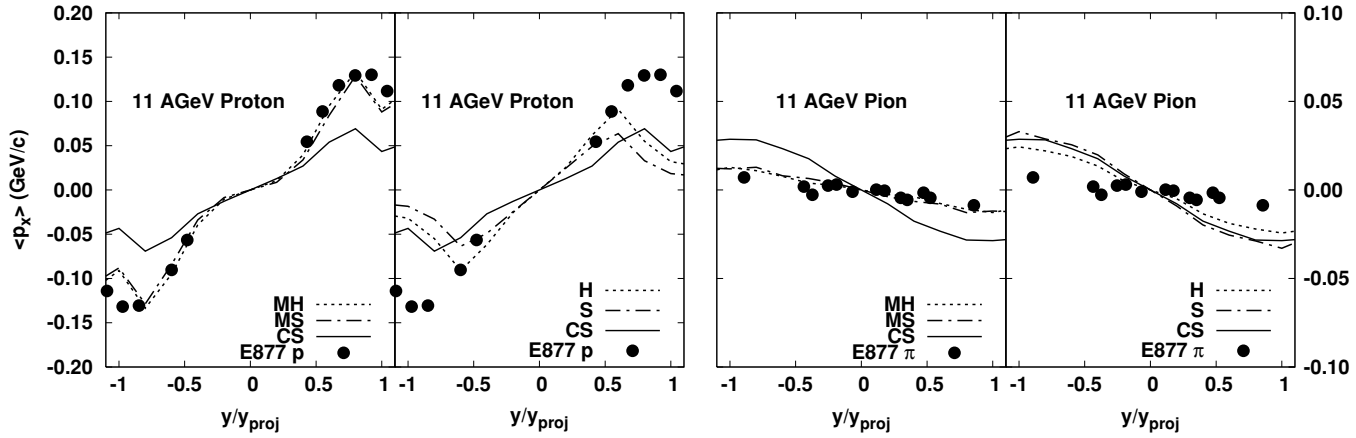

FIG. 3. Comparison of calculated sideward flow $\langle p_x \rangle$ of protons (left) and pions (right) in 11A GeV Au+Au mid-central collisions to AGS-E877 data [18]. The meaning of the curves is the same as in Fig. 2.

of $\langle p_x \rangle$ in the forward rapidity region ($y/y_{\rm proj} \simeq \pm 1$) is small compared with the data, and the slope parameters at mid-rapidity are also smaller than that of the data with soft MF. The momentum-independent soft MF reduces $\langle p_x \rangle$ in the forward rapidity region and enhances the slope parameters at mid-rapidity. The former is an unfavorable effect in explaining the data, and the latter is not enough. With momentum-independent hard (H) MF, the slope parameter is well reproduced, but the $\langle p_x \rangle$ at forward rapidities are smaller than the data, especially at $E_{\rm inc} = 2A$ and 11A GeV.

Proton sideward flow data are qualitatively reproduced with the momentum-dependent MF. The momentum-dependent MF pushes up the flow almost linearly as a function of rapidity, and it becomes closer to the data, while the $\langle p_x \rangle$ values at forward rapidities may be a little too large compared with the data at $E_{\rm inc} = (4$–$8)A$ GeV. As the incident energy increases, MF effects on the slope parameter at mid-rapidity become small, but we can still see clear differences at forward rapidities between the results with and without momentum dependence.

Our results suggest the necessity of the momentum dependence in the MF to yield large-magnitude emission in the x direction at forward rapidity. We note that our results with momentum-dependent MF are consistent with the previous calculations with MF on the collective flow data at AGS energies [25,28,33] as well as SIS energies [15,30].

The importance of momentum dependence in the MF is also seen in the transverse momentum dependence of the proton v_2 as shown in Fig. 4. Only if momentum dependence is included do we reproduce the strong squeezing at $E_{\rm inc} = 2A$ GeV of the p_T dependence.

In the right-hand panel of Fig. 3, we plot the results of sideward flow $\langle p_x \rangle$ for pions in Au+Au collisions at $E_{\rm inc} = 11A$ GeV. The sideward flow $\langle p_x \rangle$ of pions are suppressed significantly by momentum-dependent MF. This may be because pions are trailed by nucleons, which is affected by MF, giving visible differences.

B. Directed flow at SPS energies

Directed flow v_1 has been measured at SPS energies [$E_{\rm inc} = (40, 158)A$ GeV] instead of $\langle p_x \rangle$ as a function of rapidity. In Fig. 5, we compare the rapidity dependence of proton v_1 with the data in mid-central Pb+Pb collisions at $E_{\rm inc} = 40A$ and 158A GeV from the CERN-NA49 Collaboration [24], both of which are deduced by the reaction plane method (standard method). One can see that momentum-dependent MF generally improves the description of v_1.

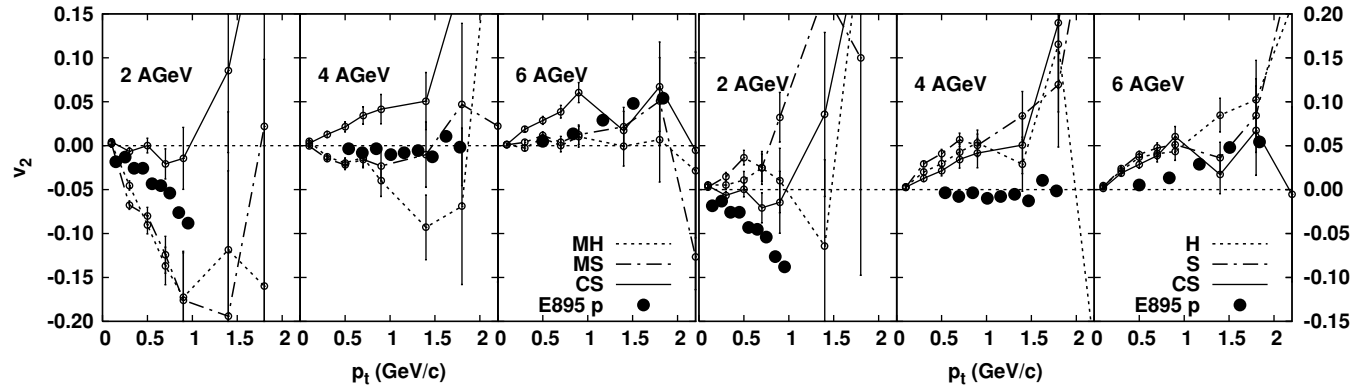

FIG. 4. Transverse momentum dependence of the elliptic flow v_2 for protons in Au+Au mid-central collisions at $(2, 4, 6)A$ GeV are compared with AGS-E895 data [20]. The meaning of the curves is the same as in Fig. 2.

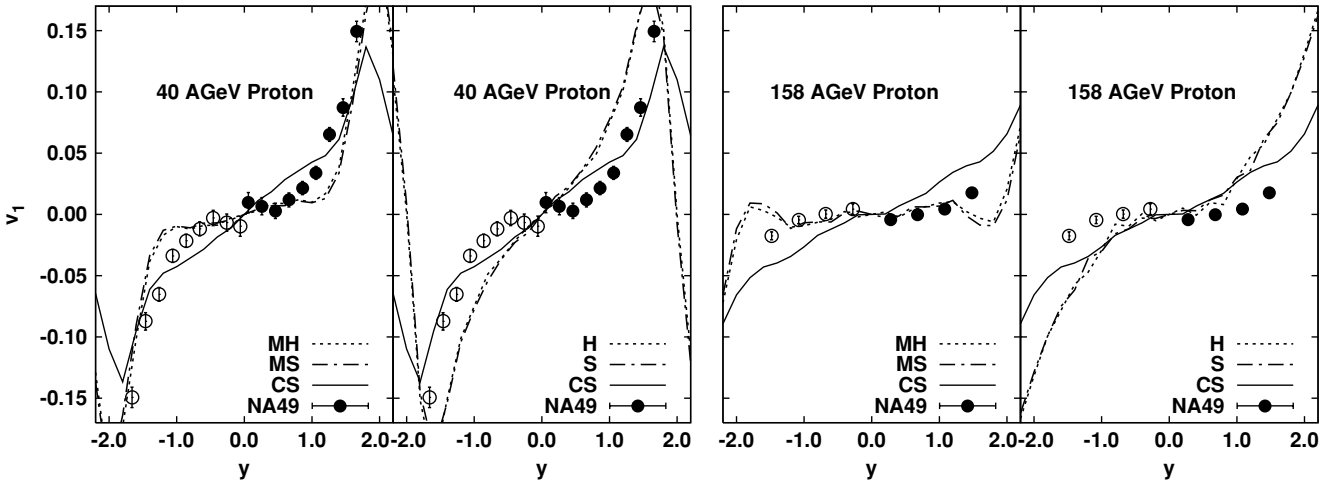

FIG. 5. Proton directed flows v_1 as a function of rapidity in mid-central Pb+Pb collisions at $E_{\rm inc} = 40A$ GeV (left panel) and $158A$ GeV (right panel) in comparison with SPS-NA49 data [24]. Curves show the calculated results of cascade with momentum-dependent hard or soft mean field (MH or MS), cascade with momentum-independent mean field (H or S), and cascade without mean field (CS).

It is interesting to note that the cascade model overestimates v_1 for protons, in contrast to the underestimate of $\langle p_x \rangle$ at AGS energies. We also see that v_1 is reduced at SPS energies with momentum-dependent MF, while $\langle p_x \rangle$ is enhanced at AGS energies. This behavior is the reverse of that at lower incident energies. Note also that the results with momentum-independent MF predict a larger v_1 than do the cascade results.

In Fig. 5 the results from the momentum-dependent MF show a flat behavior at mid-rapidity at $158A$ GeV. The wiggle (a negative slope of the proton v_1 near mid-rapidity) [29] has been reported at peripheral collisions [24]. It would be interesting to study this in detail in the future.

In Fig. 6 we compare the transverse momentum dependence of v_1 for protons in Pb+Pb collisions at $E_{\rm inc} = 40A$ and $158A$ GeV with the data. We choose rapidity cut $|y| < 1.8$ for $40A$ GeV and $|y| < 2.1$ for $158A$ GeV according to the experimental cuts. The p_T dependence at $158A$ GeV is very different from that at $40A$ GeV. Dense baryonic matter is tentatively formed in the calculations up to around $40A$ GeV, while many strings are formed and hadrons are formed later at $158A$ GeV at mid-rapidity. As a result, v_1 does not necessarily grow as a function of p_T at $158A$ GeV, because strings do not feel the MF in our model, and hadrons with large p_T from string decay have a long formation time in the total CM system, and they would have smaller chances to interact with other hadrons before strings decay.

Let us now turn to the pion v_1. We show v_1 for pions as a function of rapidity in Fig. 7 and transverse momentum in Fig. 8 at $40A$ and $158A$ GeV. It is seen that MF effects for pion v_1 are very small, especially at mid-rapidities. MF effects are seen only in the forward rapidity region for momentum-dependent MF. At $40A$ GeV, in the forward rapidity region, we find reduction (enhancement) of v_1 in the momentum-dependent (-independent) MF results compared with cascade ones. This comes from the counteraction from

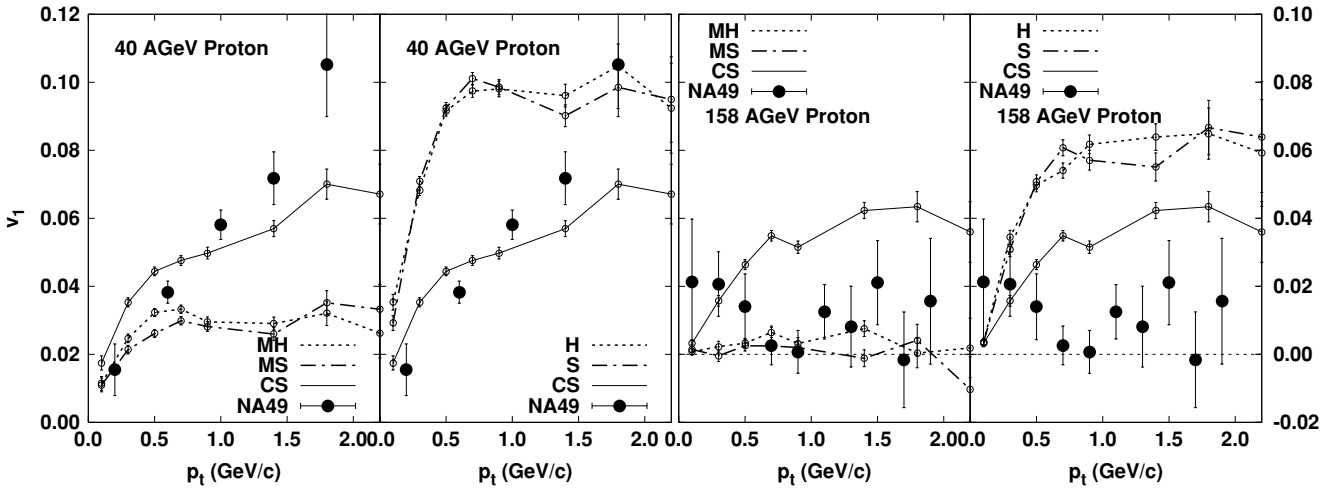

FIG. 6. Proton directed flows v_1 as a function of transverse momentum in mid-central Pb+Pb collisions at $E_{\rm inc} = 40A$ GeV (left panel) and $158A$ GeV (right panel) are compared with SPS-NA49 data [24]. The meaning of the curves is the same as Fig. 5.

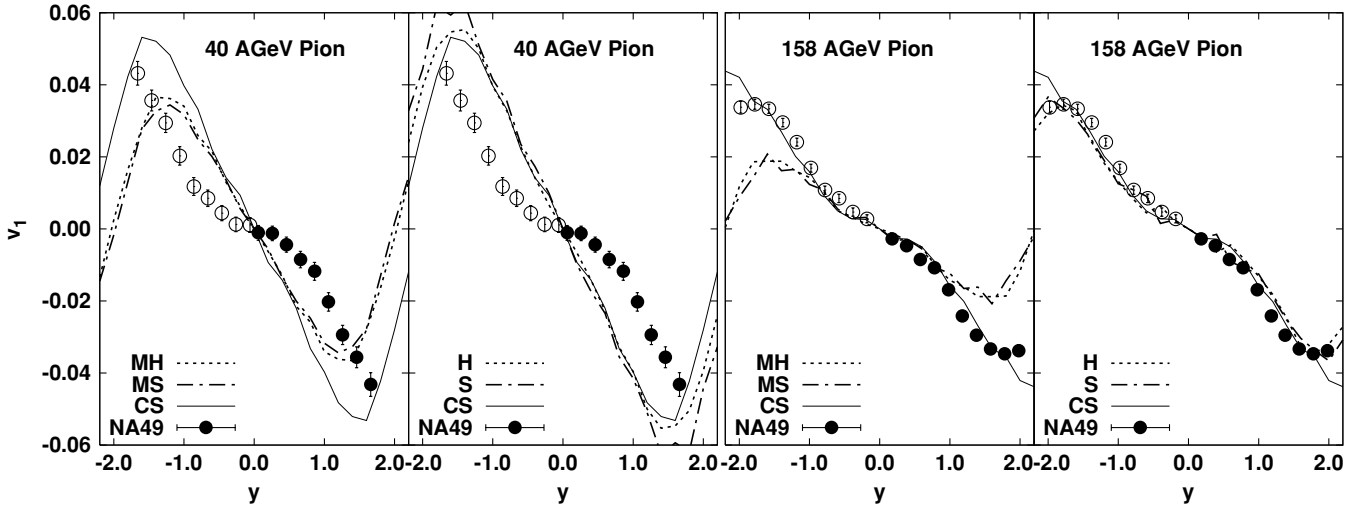

FIG. 7. Pion directed flows v_1 as a function of rapidity in mid-central Pb+Pb collisions at $E_{\rm inc} = 40A$ GeV (left panel) and 158A GeV (right panel) are compared with SPS-NA49 data [24]. The meaning of the curves is the same as Fig. 5.

protons; momentum-dependent (-independent) MF reduces (enhances) proton v_1 in the mid-rapidity region, and pion v_1 anticorrelates with proton v_1. Probably we need to include pion MF for a better understanding of the collective flows at SPS energies.

C. Elliptic flow at SPS energies

Since the v_1 signal becomes small owing to the short participant-spectator interaction time at high energies, the next Fourier coefficient, called the elliptic flow v_2, has been discussed more extensively at SPS and RHIC. At these energies, the participants form an almondlike shape in the transverse plane after the spectators go through, and these almond-shaped participants start to expand more strongly in the x (shorter axis of the almond) direction because of the higher-pressure gradient if the participants are well thermalized. This expansion is known to lead to the enhancement of in-plane particle emission, i.e., positive elliptic flow v_2.

In Figs. 9 and 10 we plot the results of the rapidity and transverse momentum dependence of v_2 for protons at SPS energies (40A and 158A GeV) together with the SPS-NA49 data [24]. At SPS energies, the cascade model generally explains the proton v_2 data qualitatively, including the flat behavior of $v_2(y)$ at mid-rapidities at 158A GeV and the approximate linear p_T dependence of $v_2(p_T)$. One exception is the missing collapse of $v_2(y)$ at mid-rapidity at 40A GeV. This collapse seen in the NA49 data may be an indication of a first-order phase transition at high baryon densities achieved in the Pb+Pb collisions at 40A GeV [34].

Effects of MF are small for proton v_2 at SPS energies. Elliptic flow is most easily generated in the early stages of the collisions, since spatial anisotropy is the largest. However, at

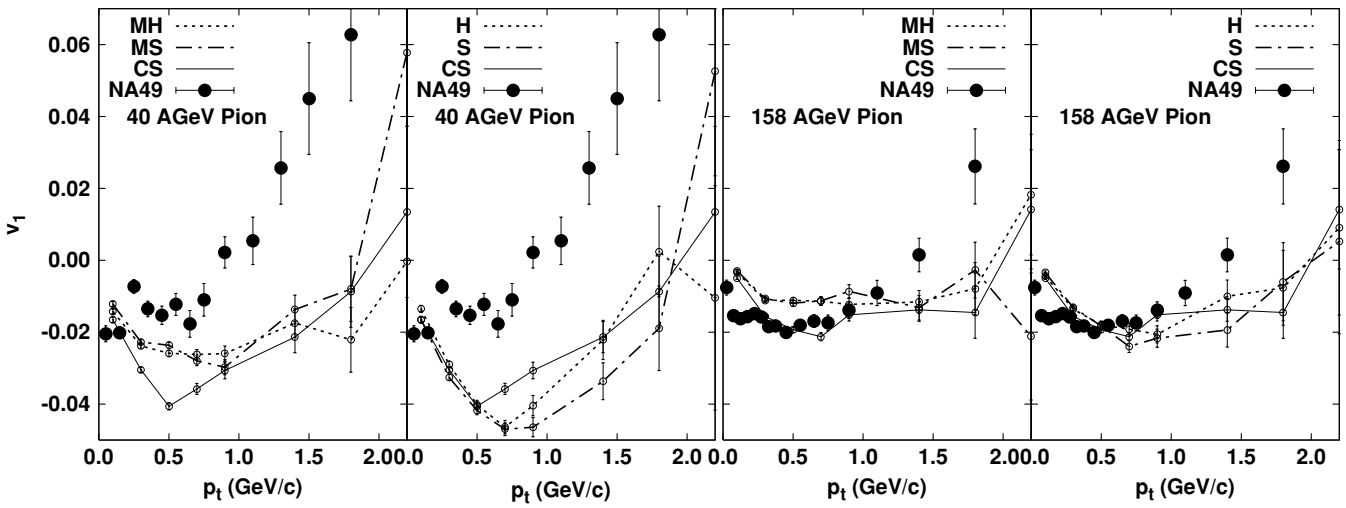

FIG. 8. Pion directed flows v_1 as a function of transverse momentum for $0 < y < 1.5$ in Pb+Pb collisions at $E_{\rm inc} = 40A$ GeV (left panel) and 158A GeV (right panel) are compared with SPS-NA49 data [24]. The meaning of the curves is the same as Fig. 5.

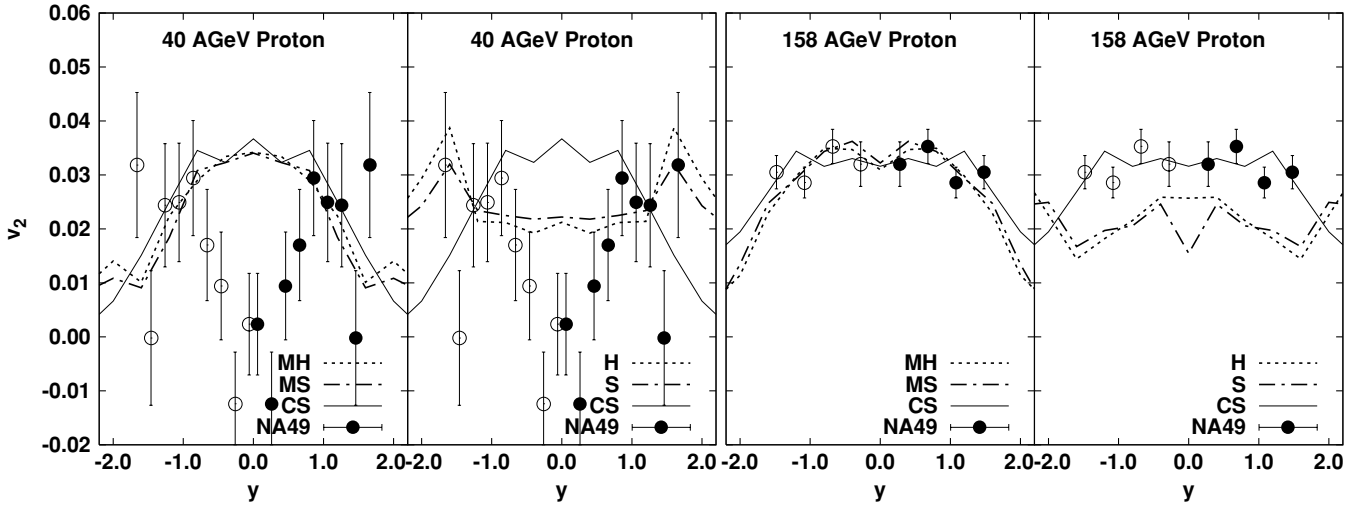

FIG. 9. Proton elliptic flows v_2 as a function of rapidity in mid-central Pb+Pb collisions at 40A GeV (left) and 158A GeV (right). Lines show the calculated results of cascade with momentum dependent hard or soft mean field (MH or MS), cascade with momentum-independent mean field (H or S), and cascade without mean field (CS). Experimental data are taken from SPS-NA49 [24].

SPS energies, string excitations dominate particle production at early times in the model, and those strings are not affected by the nuclear mean field. That is the reason that MF effects are small at SPS energies in our results.

The rapidity and the transverse momentum dependences of the pion v_2 are shown in Figs. 11 and 12, respectively. The rapidity dependence at 158A GeV and the transverse momentum dependence at low p_T ($p_T < 1$ GeV/c) at 40A and 158A GeV are well explained by the cascade model as well as by the momentum-dependent or -independent MF models, and we do not find any significant MF effects for these observables. By contrast, we do not see the collapse of $v_2(y)$ at mid-rapidities seen in the 40A GeV NA49 data, and we underestimate v_2 at high p_T. The former corresponds to the collapse of proton $v_2(y)$ mentioned before. Momentum-independent MF enhances pion $v_2(y)$ slightly, but this is in the reverse direction needed to explain the data at 40A GeV. The strong increase of $v_2(p_T)$ up to around $p_T \sim 2$ GeV/c is also seen at RHIC energies, and this behavior is discussed as an indication of hydrodynamic evolution [50].

We now turn to the discussion of the difference between v_1 and v_2. We have shown that MF effects on v_1 are rather strong, but v_2 is relatively insensitive to MF at SPS energies. This may come from the difference of developing time between v_1 and v_2. The directed flow v_1 at mid-rapidities is generated mainly by the interaction between participants and spectators in the early stage of the collision, where baryon density is the highest. On the other hand, v_2 in our model is generated in the late stage until the time reaches the order of the nuclear radius, where densities are not very high, but it is not formed in the early stage in our model. This is because our current hadronic transport approach does not have large participant

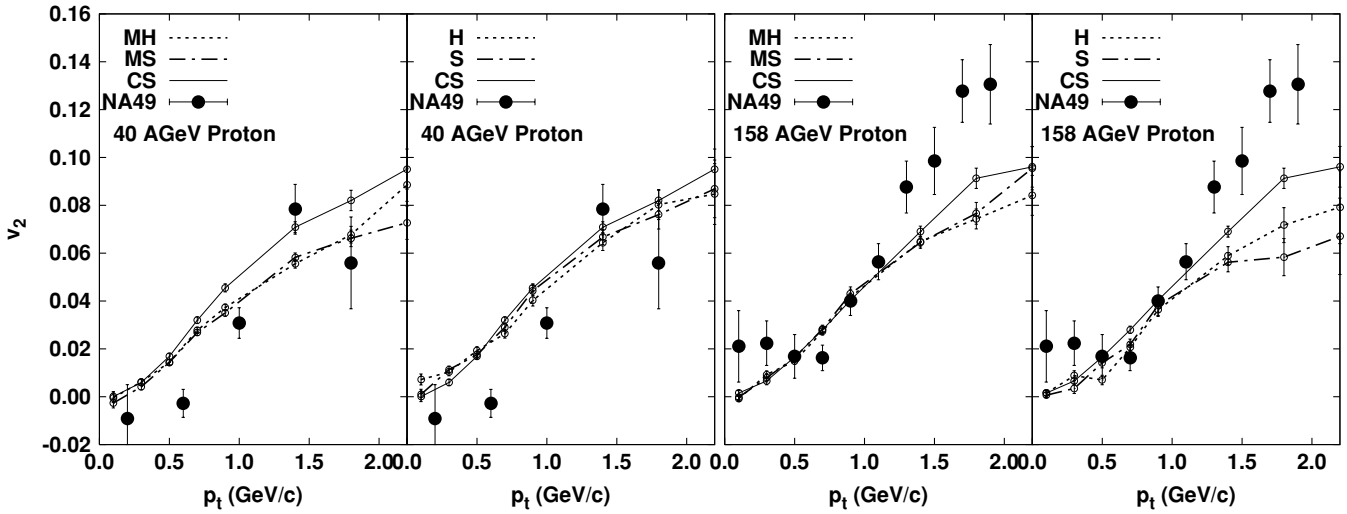

FIG. 10. Proton elliptic flows v_2 as a function of transverse momentum. The meaning of the curves is the same as Fig. 9.

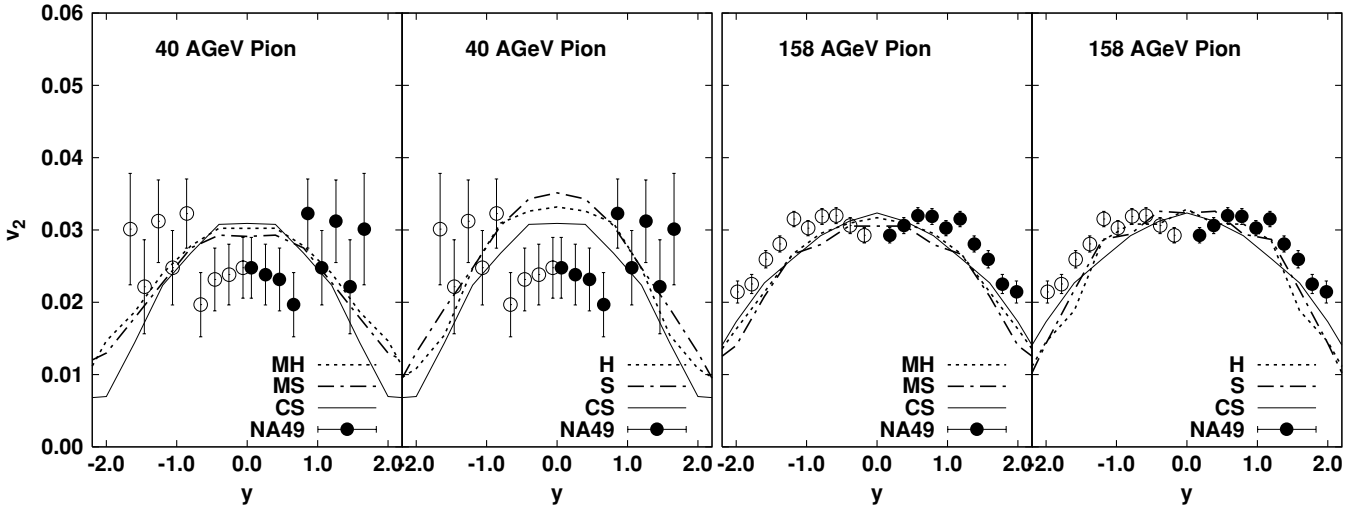

FIG. 11. Pion elliptic flows v_2 as a function of rapidity. The meaning of the curves is the same as Fig. 9.

pressure in the early stages of the collisions, as we do not explicitly include MF for strings and partonic interactions. In a hydrodynamic picture, v_2 develops from very early times owing to thermal pressure. This is a striking difference between our approach and hydrodynamics, as was previously studied in Ref. [41].

D. Elliptic flow excitation functions from AGS to SPS energies

When the incident energy is not high enough, spectators squeeze participants out of the reaction plane owing to the repulsive nuclear interactions at $0.2A \lesssim E_{\rm inc} \lesssim 4A$ GeV. This squeezing leads to a negative value of the elliptic flow of nucleons ($v_2 < 0$). The elliptic flow, therefore, shows the strength of the repulsive interaction at lower energies. On the other hand, elliptic flow becomes positive at higher energies, because there is no such squeezing effect that is due to the Lorentz contraction. Elliptic flow gives a information how much pressure is generated at higher energies.

In Fig. 13 we show the incident energy dependence of proton v_2 in mid-central collisions with measured data [$-0.1 < y < 0.1$ for AGS, $0 < y < 2.1 (0 < y < 1.8)$ for SPS 158A (40A) GeV] [19,24]. Rapidity cut $|y| < 0.2 y_{\rm proj}$ has been used in the calculations. Experimental data clearly show the evolution from squeezing to almond-shaped participant dynamics. With both cascade and momentum-independent soft MF (S), we cannot explain strong squeezing effects at lower energies. The calculated v_2 values for momentum-independent MF (H, S) and cascade are generally larger than data at AGS energies. Momentum-dependent MF (MH, MS), which is repulsive in the incident energy range under consideration, pushes down the elliptic flow significantly. We qualitatively reproduce the incident energy dependence from AGS [19] to SPS [24] energies.

Calculated results with both MH and MS are smooth as a function of beam energy, while the data at $E_{\rm inc} = 40A$ GeV has a dip [24]. Confirmation of data is necessary to examine the incident energy dependence of v_2, whether it is a monotonic

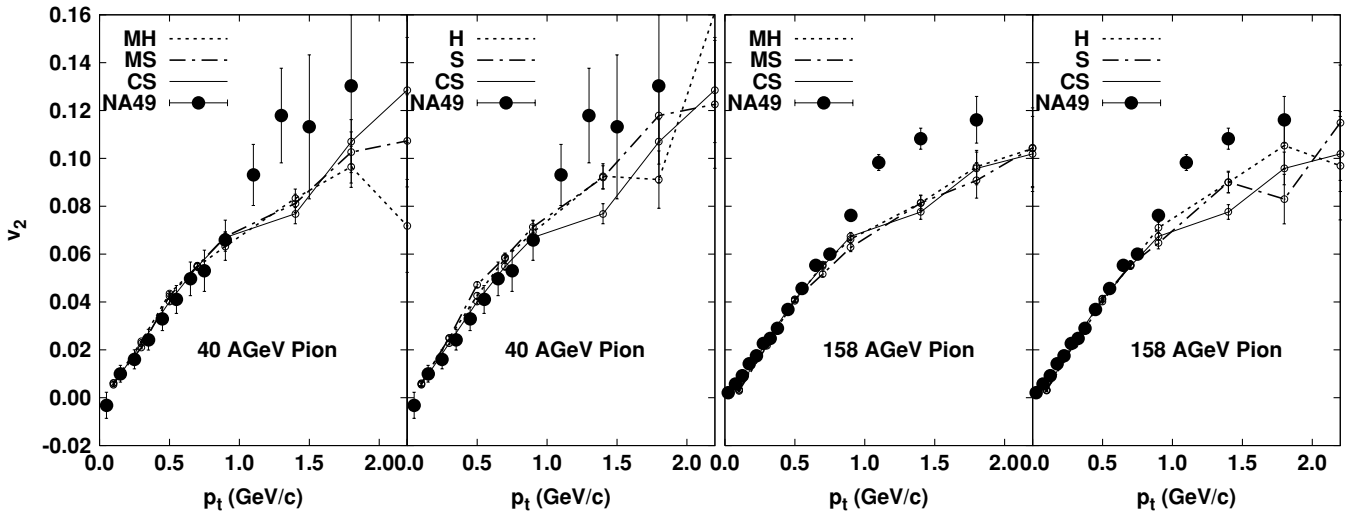

FIG. 12. Pion elliptic flow v_2 as a function of transverse momentum. The meaning of the curves is the same as Fig. 9.

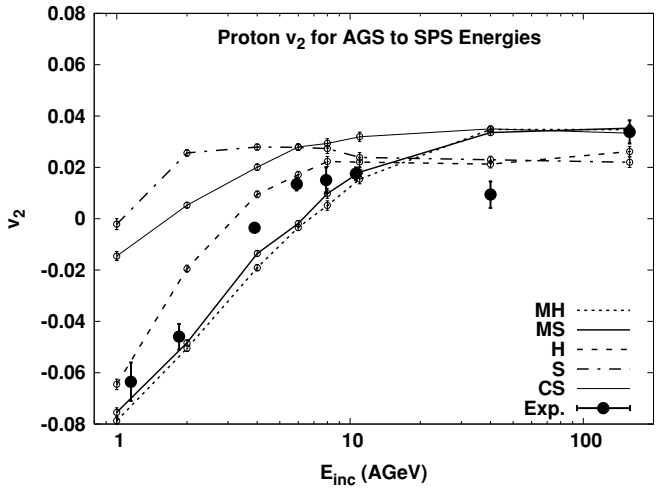

FIG. 13. Incident energy dependence of proton elliptic flow at mid-rapidities in mid-central heavy-ion collisions from 1*A* GeV to 158*A* GeV. Dotted, bold-solid, dashed, and dotted-dashed and thin-solid lines show the results of cascade with MH, MS, H, S mean-field, and cascade without mean-field (CS), respectively. The experimental data are taken from LBL-EOS, AGS-E895, E877 from Ref. [19], and SPS-NA49 from Ref. [24].

function or has a dip at around $E_{\rm inc} \sim 40A$ GeV, by looking at the missing data points.

In our results with momentum-dependent potentials, the stiffness dependence of v_2 is smaller than that in the Boltzmann equation model (BEM) [19,27,28]. In the RQMD/S framework with the relativistic distance $\tilde{\boldsymbol{r}}_{ij}^2$, the interaction between the projectile and target nucleons are suppressed at high energies by the factors m_i/p_i^0 and m_j/p_j^0 in the potential derivatives in Eqs. (A25) and (A26). For momentum-dependent potentials, we have the relative momentum vector $\boldsymbol{p}_{ij}$ in Eq. (A29), which can compensate for the suppression factor in Eq. (A26). For momentum-independent potentials, on the other hand, the pair velocity $\boldsymbol{\beta}_{ij}$ in Eq. (A20) is very small for nucleon pairs between the projectile and target, and there is no enhancement factor to compensate for the above suppression in the derivatives of the relativistic distance $\tilde{\boldsymbol{r}}_{ij}^2$ in Eqs. (A27) and (A28). This suppression does not happen in BEM, and they find significant stiffness dependence in Refs. [19,27,28], while we do not see strong stiffness dependence. In the case of momentum-independent potentials, our results are closer to the cascade results compared with those in Refs. [48,58]. This difference also comes from the above suppression between the projectile and target nucleons. The essential reason for these differences is that in RQMD or RQMD/S potentials are regarded as Lorentz scalar. Possible other model dependences will be discussed in the next section.

IV. MODEL UNCERTAINTIES

In the previous section it has been shown that the momentum-dependent hard or soft MF improved the description of the collective flow data from AGS to SPS energies. However, there are some uncertainties in our calculations for the study of collective flows.

First, let us consider the effects of the MF for nonnucleonic baryons. Strange baryons, resonance hadrons, or antibaryons are expected to feel MF, which may be different that affecting nucleons. In the previous section we assumed that all the baryons feel the same MF, and this treatment would give a rough estimate of a maximum MF effect, since, for example, the MF for Δ's or Λ's is generally expected to be smaller than that for nucleons. On the other hand, if we include MF only for nucleons, we may get a rough estimate of a minium baryonic MF effects.

In Figs. 14 and 15, we compare the results with and without MF for nonnucleonic baryons. We can read in the left-hand panel of Fig. 14 that ignoring MF for nonnucleonic baryons (specified as N in the figure) at 2*A* GeV reduces both the $\langle p_x \rangle$ slope and the strength at the forward rapidities by about 20% compared with the case of B, in which all baryons feel MF. But the slope remains the same at 11*A* GeV for N and B. On the other hand, it is seen in the right-hand panel of Fig. 14

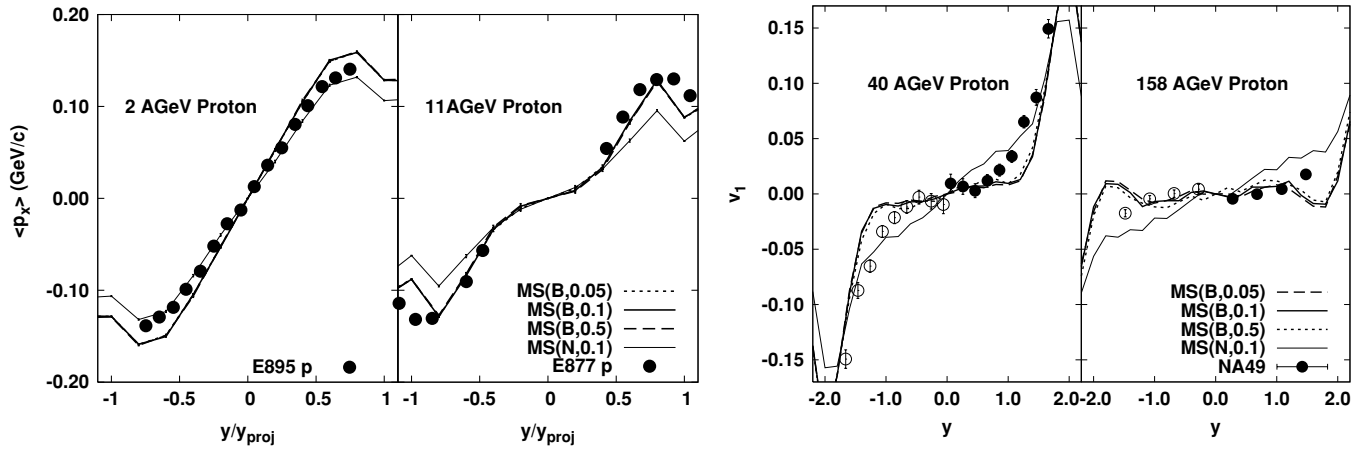

FIG. 14. Sideward (directed) flows of AGS (left) and SPS (right) energies are compared with different assumptions for the mean fields. The momentum-dependent soft (MS) mean-field has been used in these calculations. The first term in the parenthesis means that all baryons (B) or only nucleons (N) are included for the MF. The second term (0.05/0.1/0.5) denotes simulation time step size *dt* (fm/*c*).

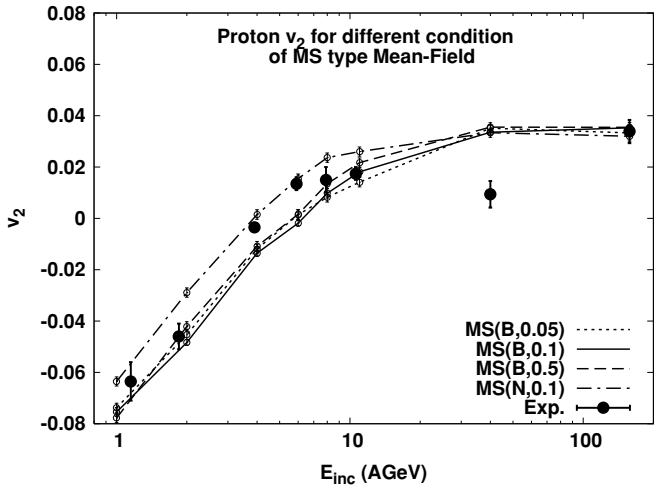

FIG. 15. Elliptic flows are compared with different assumptions for the mean fields. The meaning of the curves is the same as Fig. 14.

that MF only for nucleons is not enough to suppress v_1 at SPS energies. One can also see some differences of v_2 in B and N in Fig. 15 up to AGS energies. The experimental data lie between B and N except for 40*A* GeV, suggesting that the MF for excited baryons is smaller than that for nucleons.

Next, we have checked the time step size dt dependence. Since the update of MF after each collision requires a huge calculation time, we evaluate MF only at each time slice. When a baryon collides in one time step, that baryon is propagated with MF until the collision time, and we ignore the MF after the collision before it is formed. In the time step of baryon formation, displacements by the MF for $\boldsymbol{p}_i$ and $\boldsymbol{r}_i$ are evaluated by using the MF at the next time slice. This treatment is valid up to the first order in dt when one baryon collides or is formed once in one time step. In the later stages this prescription is expected to work well because of the low collision frequency. In the early stages many collisions make strings and resonances, which do not feel MF, so our prescription may not be too bad. In the middle stages, however, it may be possible that elastic scatterings are frequent enough and baryons continue to feel MF after collisions in each time step. Thus we need to analyze the collision frequency effects on constructing flows by reducing dt. In Figs. 14 and 15 we plot the results with different time step sizes $dt = 0.05$, 0.1, 0.5 fm/c. For $\langle p_x \rangle$ at AGS energies (left-hand panel of Fig. 14), all the results with different time step size agree well with each other, and we cannot distinguish these lines. The time step size dependence of v_2 as shown in Fig. 15 still gives us confirmation of the convergence of the numerical results. For v_1 at SPS energies (right-hand panel of Fig. 14), only very small differences can be seen between the results with $dt = 0.5$ fm/c and $dt \leqslant 0.1$ fm/c. We conclude that $dt = 0.1$ fm/c, which has been used as a default throughout this work, is small enough to perform a reliable calculations.

Finally, we would like to address the problem of the uncertainties of the transport model itself. In addition to the ambiguities in introducing collision terms, the equations of motion depend on the model treatment. It is not trivial at all to construct equations of motion of relativistic particles during heavy-ion collisions based on the potential or the MF, giving an appropriate EOS. At relativistic energies there are proposed several ways to introduce the potential effects.

(i) Relativistic mean field (RMF), having Lorentz scalar U_s and vector U_v^μ terms (RBUU [25,32]). The scalar and the vector time component are evaluated in the local rest frame, and by the Lorentz transformation we can get U_v^μ in the calculation frame. Thus, neglecting a nonlocality in time, this evaluation of the potential is practically covariant. In this approach, however, we need to introduce strong cutoff for the coupling of vector meson and baryons [25], since the vector potential effects linearly increase as a function of incident energy.

(ii) Lorentz scalar reinterpretation of nonrelativistic potentials (BUU [31], BEM [27]). In the BUU model [31] the Lorentz scalar MF U_s is obtained from the nonrelativistic MF U in the local rest frame through the relation

$$\begin{aligned}\varepsilon(\boldsymbol{p}, \rho) &= \sqrt{[m + U_s(\boldsymbol{p}, \rho)]^2 + \boldsymbol{p}^2} \\ &= \sqrt{m^2 + \boldsymbol{p}^2} + U(\boldsymbol{p}, \rho),\end{aligned} \tag{10}$$

where ρ is the baryon density [31]. For the momentum-independent MF in BEM in Refs. [27,28], the scalar potential is directly given so as to fit the EOS, and the scalar density is used for ρ. They do not have any vector terms increasing at high energies, and the potential effects become mild compared with the RMF treatment. For example, the derivative of the above single-particle energy gives rise to the factor $(m + U_s)/\varepsilon$ in front of the U_s derivative and suppresses the potential effects.

(iii) Combination of the Lorentz scalar and nonrelativistic-type density-dependent potentials (BEM [26–28]). This approach is adopted in Ref. [26] and in the momentum-dependent MF in Refs. [27,28]. The single-particle energy is given as

$$\varepsilon(p, \rho) = m + \int_0^p dp' v^*(p', \rho) + \widetilde{U}(\rho), \tag{11}$$

$$v^*(p, \rho) = \frac{p}{\sqrt{p^2 + [m^*(p, \rho)]^2}}. \tag{12}$$

The derivative of $\widetilde{U}(\rho)$ does not come with a suppression factor such as m/ε, and it generates strong effects at high energies, where both the density and the density derivative become large.

(iv) Constraint Hamiltonian dynamics (RQMD [39], RQMD/S [43]). In RQMD and RQMD/S, particle velocity and force are not given by the derivatives of the single-particle energy but by the derivatives of the total Hamiltonian, as shown in the Appendix in the case of RQMD/S. Thus the relation to other MF models described above is not straightforward. However, the potential V_i in the on-mass-shell constraint (A8) is introduced as Lorentz scalar, and we have suppression factor m/p^0 in the equations of motion, (A14) and (A15). These observations suggest that the RQMD and RQMD/S would give results similar to those in Lorentz scalar MF models, such as BUU [31]. Another difference from other MF models exists in the

nuclear density profile. One nucleon is represented by one Gaussian packet rather than many test particles, then the nuclear diffuseness becomes generally larger in QMD-type models. This may generate artificial surface effects at large impact parameters or in light-ion collisions. However, central and mid-central collisions of heavy-nuclei are expected to be well described, as in the case of various cascade models, in which one particle is used for one hadron.

We are not very sure which is the best way to include the potential effects in high-energy heavy-ion collisions. Further formal developments on transport models in relation to the nuclear EOS would be necessary, and at the same time, phenomenological studies of heavy-ion collisions are required in order to verify the validity of models and to elucidate the EOS. From the latter point of view, systematic study in wide range of incident energy is needed, since the above uncertainties are closely related to the Lorentz transformation properties, whose effects would vary drastically as the incident energy varies. The incident energy range from AGS to SPS energies studied in this work may provide a good benchmark test for transport models and the EOS.

V. SUMMARY

We have investigated collective flows in heavy-ion collisions from AGS [(2–11)A GeV] to SPS [(40, 158)A GeV] energies by using a combined framework of hadron-string cascade (JAM) [49] and covariant constraint Hamiltonian dynamics (RQMD/S) [43]. In JAM, various particle production mechanisms are taken into account — production and decay of resonances and strings, jet production, and its fragmentation. Momentum dependence of the MF is fitted [55] to the real part of the Schrödinger equivalent global optical potential of Hama *et al*. [38] in a Lorentzian form, Eq. (1). Saturation properties are fitted by introducing the density-dependent potential of the Skyrme type in the power series of ρ. Calculated results of cascade, cascade with momentum-dependent MF, and cascade with momentum-independent MF are compared with the data of sideward $\langle p_x \rangle$, directed v_1, and elliptic v_2 flows as a function of rapidity, transverse momentum, and beam energy from AGS to SPS. Generally, results with momentum-dependent MF explain the trend of the data for proton flows reasonably well. We note that this is the first that the anisotropic proton collective flow data of heavy-ion collisions from AGS to SPS has been explained in one framework consistently. Without momentum dependence in MF, we cannot reproduce the strong enhancement of the sideward flow at $E_{\rm inc} = (2\text{–}11)A$ GeV, strong squeezing seen in v_2 for $E_{\rm inc} \lesssim 4A$ GeV, and the suppression of proton v_1 at $E_{\rm inc} = 40A$ and $158A$ GeV.

Our new model—a hadron-string cascade with momentum-dependent MF—provides an improved description for collective flows in mid-central collisions from AGS to SPS energies. The present analysis implies that the effects of the momentum-dependent potential is large up to the SPS energies.

There are still many problems in the attempt to pin down the equation of state of dense nuclear matter from heavy-ion data. First, we have made an assumption that the MF is taken into account only for baryons and that all the baryons feel the same MF. It would be interesting to extend the present work to discuss the MF effects for mesons and different MFs for hyperons and resonance hadrons and to look at the Λ or kaon flow data. Second, we cannot make the soft EOS ($K \sim 200$ MeV) with the present form of the MF be consistent with the optical potential. When the momentum dependence is fitted to the optical potential by Hama *et al*. [38] in the Lorentzian form, the EOS necessarily becomes relatively stiff in combination with the Skyrme-type density-dependent form, as shown in Table I. The small sensitivity of the EOS to momentum in this work may suggest that the probed EOS range is not wide enough. Finally, the model dependence of the MF treatment has to be removed in order to obtain model-independent EOS information. For this purpose it is necessary to test various MF treatments in one framework. In the present model, we need to modify the on-mass-shell constraint to include Lorentz vector potentials or potentials of other types. It can be a breakthrough for a transport model-independent discussion of the EOS.

ACKNOWLEDGMENTS

We are grateful to Professor Tomoyuki Maruyama and Professor Pawel Danielewicz for useful discussions and comments. This work is supported in part by the Ministry of Education, Science, Sports and Culture, Grand-in-Aid for Scientific Research (C)(2), no. 15540243, 2003.

APPENDIX: RQMD/S FORMALISM

Here we briefly summarize the RQMD/S formalism developed by Maruyama *et al*. in Ref. [43] for completeness. The original RQMD formalism is initiated by Sorge *et al*. in Ref. [39]. RQMD(/S) is based on the constrained Hamiltonian dynamics [59], which is formulated in a manifestly covariant way. We use four-vectors q_i^μ and p_i^μ for the description of the N particle system. Therefore we need to have $2N$ constrains $\phi_i (i = 1, \ldots, 2N)$, as physical phase space is $6N$ dimensional. Now our Hamiltonian may be constructed from the constraints ϕ_i, and the Lagrange multiplier u_i from the Dirac's constraint Hamiltonian formalism:

$$H = \sum_{i=1}^{2N-1} u_i \phi_i . \tag{A1}$$

The equations of motion are then

$$\frac{dq_i}{d\tau} = \{H, q_i\} \approx \sum_{j=1}^{2N-1} u_j \frac{\partial \phi_j}{\partial p_i}, \tag{A2}$$

$$\frac{dp_i}{d\tau} = \{H, p_i\} \approx -\sum_{j=1}^{2N-1} u_j \frac{\partial \phi_j}{\partial q_i}, \tag{A3}$$

where the Poisson brackets are defined as

$$\{A, B\} \equiv \sum_{k,\mu} \left(\frac{\partial A}{\partial q_k^\mu} \frac{\partial B}{\partial p_{k\mu}} - \frac{\partial A}{\partial p_{k\mu}} \frac{\partial B}{\partial q_k^\mu} \right), \tag{A4}$$

$$\left\{q_i^\mu, p_{j\nu}\right\} = \delta_\nu^\mu \delta_{ij}, \quad \left\{q_i^\mu, q_j^\nu\right\} = 0, \quad \left\{p_{i\mu}, p_{j\nu}\right\} = 0, \\ i, j, k = 1, \ldots, N, \quad \mu, \nu = 0, 1, 2, 3, \tag{A5}$$

and the sign $\approx$ means the weak equality initiated by Dirac [60]. When we require that constraints ϕ_i should be conserved in time, then they fulfill

$$\frac{d\phi_i}{d\tau} = \frac{\partial \phi_i}{\partial \tau} + \sum_{j=1}^{2N-1} u_j \{\phi_i, \phi_j\} \approx 0. \tag{A6}$$

Particle trajectories in $6N$ phase space is uniquely determined by the equations of motion Eqs. (A2) and (A3) together with Eqs. (A10) and (A11) when $2N$ constraints are given.

We use the following $2N$ constraints in RQMD/S

$$\phi_i \equiv \begin{cases} H_i & i = 1, \ldots, N \\ \chi_{i-N} & i = N+1, \ldots, 2N. \end{cases} \tag{A7}$$

First N constraints are the on-mass-shell constraints

$$H_i \equiv p_i^2 - m_i^2 - 2m_i V_i \approx 0, \quad i = 1, \ldots, N. \tag{A8}$$

Remaining N conditions constrain the time fixation of the particles. In the original RQMD time fixation [39,40,42], the $N \times N$ matrix has to be solved numerically at each time step to deduce inverse matrices. Moreover, if particle production or annihilation occurs, the time fixation is violated, and a initial q_i of produced particles satisfying the constraints and energy conservation has to be imposed.

Maruyama *et al.* introduced a simplified time fixation in RQMD/S with the global time parameter τ in Ref. [43], as

$$\chi_i \equiv \hat{a} \cdot (q_i - q_N) \approx 0, \quad i = 1, \ldots, N-1, \\ \chi_N \equiv \hat{a} \cdot q_N - \tau \approx 0, \tag{A9}$$

where $\hat{a}$ is a four-component vector corresponding to $(1, \mathbf{0})$ at the rest frame of the particle and q_i is space-time coordinate of the ith particle. The constraints equation (A9) can be satisfied in the case of particle production.

Since the constraint $\phi_i (i = 1, \ldots, 2N-1)$ does not depend explicitly on τ, the Lagrange multiplier $u_i(\tau)$ can be solved as

$$u_i \approx -\frac{\partial \phi_{2N}}{\partial \tau} C_{2N,i}, \quad i = 1, \ldots, 2N-1, \tag{A10}$$

where

$$C_{ij}^{-1} \equiv \{\phi_i, \phi_j\}, \quad i, j = 1, \ldots, 2N. \tag{A11}$$

The matrix C (inverse of matrix C^{-1}) must exist, because we only allow for the τ-dependent $2N$th constraint functions, which are combined with the $2N-1$ constraints. Furthermore, C can be obtained analytically, if we replace p_i^0 from the potential V_i with the kinetic energy $\sqrt{\boldsymbol{p}_i^2 + m_i^2}$. This is a great advantage from the point of view of CPU time. One obtains the RQMD/S Hamiltonian

$$H \approx \sum_{i=1}^{N} u_i \left(p_i^2 - m_i^2 - 2m_i V_i\right), \tag{A12}$$

where

$$u_i = \frac{1}{2p_i^0}, \quad p_i^0 = \sqrt{\boldsymbol{p}_i^2 + m_i^2 + 2m_i V_i}. \tag{A13}$$

The equations of motion are then

$$\frac{d\boldsymbol{r}_i}{d\tau} \approx -\frac{\partial H}{\partial \boldsymbol{p}_i} = \frac{\boldsymbol{p}_i}{p_i^0} + \sum_{j=1}^{N} \frac{m_j}{p_j^0} \frac{\partial V_j}{\partial \boldsymbol{p}_i}, \tag{A14}$$

$$\frac{d\boldsymbol{p}_i}{d\tau} \approx \frac{\partial H}{\partial \boldsymbol{r}_i} = -\sum_{j=1}^{N} \frac{m_j}{p_j^0} \frac{\partial V_j}{\partial \boldsymbol{r}_i}. \tag{A15}$$

In actual calculations, we have replaced p_i^0 with the kinetic energy $\sqrt{\boldsymbol{p}_i^2 + m_i^2}$ in the denominators of Eqs. (A14) and (A15) after evaluating all the derivative terms for simplicity. This approximation would be valid in the relativistic energy region, where the kinetic energy is much larger than the potential V_i.

Relative distance $\boldsymbol{r}_{ij} = \boldsymbol{r}_i - \boldsymbol{r}_j$ and $\boldsymbol{p}_{ij} = \boldsymbol{p}_i - \boldsymbol{p}_j$ in the potentials should be replaced by the squared four-vector distance with a Lorentz scalar, as

$$-{q_{Tij}}^2 = -{q_{ij}}^2 + \frac{(q_{ij} \cdot P_{ij})^2}{{P_{ij}}^2}, \tag{A16}$$

$$-{p_{Tij}}^2 = -{p_{ij}}^2 + \frac{(p_{ij} \cdot P_{ij})^2}{{P_{ij}}^2}, \tag{A17}$$

where $p_{ij} = p_i - p_j, q_{ij} = q_i - q_j, \quad P_{ij} = p_i + p_j$. We note that in the nonrelativistic limit $-{q_{Tij}}^2 \overrightarrow{_{c\to\infty}} \boldsymbol{r}_{ij}^2$. This assumption takes into account the contraction of longitudinal direction, and we can avoid unphysical compression. In the actual simulations, we use the following expression:

$$-q_{Tij}^2 \equiv \tilde{\boldsymbol{r}}_{ij}^2 = \boldsymbol{r}_{ij}^2 + \gamma_{ij}^2 (\boldsymbol{r}_{ij} \cdot \boldsymbol{\beta}_{ij})^2, \tag{A18}$$

$$-p_{Tij}^2 \equiv \tilde{\boldsymbol{p}}_{ij}^2 = \boldsymbol{p}_{ij}^2 - \left(p_i^0 - p_j^0\right)^2 + \gamma_{ij}^2 \left(\frac{m_i^2 - m_j^2}{p_i^0 + p_j^0}\right)^2, \tag{A19}$$

where the velocity and the γ factor between the ith and the jth particle are given by

$$\boldsymbol{\beta}_{ij} = \frac{\boldsymbol{p}_i + \boldsymbol{p}_j}{p_i^0 + p_j^0}, \quad \gamma_{ij} = \frac{1}{\sqrt{1 - \boldsymbol{\beta}_{ij}^2}}. \tag{A20}$$

We now write the explicit form of the equations of motion in RQMD/S, which is used in the actual simulation. As explained in Sec. II, we use the following potentials:

$$V = \sum_i (V_{\text{Sky}\,i} + V_{\text{mom}\,i}) \\ = \sum_i \left[\frac{\alpha}{2\rho_0} \langle \rho_i \rangle + \frac{\beta}{(1+\gamma)\rho_0^\gamma} \langle \rho_i \rangle^\gamma \right. \\ \left. + \sum_{k=1,2} \frac{C_{\text{ex}}^{(k)}}{2\rho_0} \sum_{j(\neq i)} \frac{1}{1 + [\tilde{\boldsymbol{p}}_{ij}/\mu_k]^2} \rho_{ij} \right], \tag{A21}$$

where $\langle\rho_i\rangle$ is obtained from a convolution of the Gaussian wave packet:

$$\langle\rho_i\rangle \equiv \sum_{j(\neq i)} \int d\boldsymbol{r}\rho_i(\boldsymbol{r})\rho_j(\boldsymbol{r}) = \sum_{j(\neq i)} \rho_{ij} = \sum_{j(\neq i)} \frac{1}{(4\pi L)^{\frac{3}{2}}} \exp\left(-\frac{\tilde{\boldsymbol{r}}_{ij}^2}{4L}\right). \tag{A22}$$

The width parameters $L = 2.05$(MH), 2.1(MS), 1.08(H and S) fm^2 are taken from Refs. [55,56]. The equations of motion (A14) and (A15) then become

$$\frac{d\boldsymbol{r}_i}{d\tau} = \frac{\boldsymbol{p}_i}{p_i^0} + \sum_{j(\neq i)} D_{ij} \frac{\partial \tilde{\boldsymbol{r}}_{ij}^2}{\partial \boldsymbol{p}_i} + \sum_{j(\neq i)} E_{ij} \frac{\partial \tilde{\boldsymbol{p}}_{ij}^2}{\partial \boldsymbol{p}_i}, \tag{A23}$$

$$\frac{d\boldsymbol{p}_i}{d\tau} = -\sum_{j(\neq i)} D_{ij} \frac{\partial \tilde{\boldsymbol{r}}_{ij}^2}{\partial \boldsymbol{r}_i}, \tag{A24}$$

where

$$D_{ij} = \left(-\frac{1}{2L}\right)\rho_{ij}\left[\frac{\alpha}{2\rho_0}\left(\frac{m_i}{p_i^0}+\frac{m_j}{p_j^0}\right) + \frac{\gamma}{1+\gamma}\frac{\beta}{\rho_0^\gamma}\left\{\frac{m_i}{p_i^0}\langle\rho_i\rangle^{\gamma-1} + \frac{m_j}{p_j^0}\langle\rho_j\rangle^{\gamma-1}\right\}\right] + \left(-\frac{1}{4L}\right)\frac{1}{2\rho_0}\rho_{ij}\left(\frac{m_i}{p_i^0}+\frac{m_j}{p_j^0}\right)\sum_{k=1,2}\frac{C_{\rm ex}^{(k)}}{1+[\tilde{\boldsymbol{p}}_{ij}/\mu_k]^2}, \tag{A25}$$

$$E_{ij} = \frac{1}{2\rho_0}\rho_{ij}\left(\frac{m_i}{p_i^0}+\frac{m_j}{p_j^0}\right)\sum_{k=1,2}\left(-\frac{1}{{\mu_k}^2}\right)\frac{C_{\rm ex}^{(k)}}{1+(\tilde{\boldsymbol{p}}_{ij}/\mu_k)^2}. \tag{A26}$$

The result of the differentials are [61]

$$\frac{\partial \tilde{\boldsymbol{r}}_{ij}^2}{\partial \boldsymbol{p}_i} = \frac{2\gamma_{ij}^2}{p_i^0+p_j^0}(\boldsymbol{r}_{ij}\cdot\boldsymbol{\beta}_{ij})\left\{\boldsymbol{r}_{ij} + \gamma_{ij}^2(\boldsymbol{r}_{ij}\cdot\boldsymbol{\beta}_{ij})\left(\boldsymbol{\beta}_{ij} - \frac{\boldsymbol{p}_i}{p_i^0}\right)\right\}, \tag{A27}$$

$$\frac{\partial \tilde{\boldsymbol{r}}_{ij}^2}{\partial \boldsymbol{r}_i} = 2\boldsymbol{r}_{ij} + 2\gamma_{ij}^2(\boldsymbol{r}_{ij}\cdot\boldsymbol{\beta}_{ij})\boldsymbol{\beta}_{ij}, \tag{A28}$$

$$\frac{\partial \tilde{\boldsymbol{p}}_{ij}^2}{\partial \boldsymbol{p}_i} = 2\boldsymbol{p}_{ij} - 2\left(p_i^0 - p_j^0\right)\frac{\boldsymbol{p}_i}{p_i^0} + 2\gamma_{ij}^4\frac{1}{p_i^0+p_j^0}\left(\frac{m_i^2-m_j^2}{p_i^0+p_j^0}\right)^2\left(\boldsymbol{\beta}_{ij} - \frac{\boldsymbol{p}_i}{p_i^0}\right). \tag{A29}$$

Finally, let us check the nonrelativistic limit to confirm the validity of Eqs. (A12)–(A15). We define the kinetic energy as $\mathcal{E}_i \equiv p_i^0 - m_i c^2$ (here we write the speed of light c explicitly), Indeed Hamiltonian (A12) and the equations of motion have the correct nonrelativistic limit, as

$$H \approx \sum_{j=1}^N \frac{1}{2}\frac{1}{\mathcal{E}_j/c^2+m_j}\left(\frac{\mathcal{E}_j^2}{c^2} + 2m_j\mathcal{E}_j - \boldsymbol{p}_j^2 - 2m_jV_j\right) \underset{c\to\infty}{\approx} \sum_{j=1}^N\left(\mathcal{E}_j - \frac{\boldsymbol{p}_j^2}{2m_j} - V_j\right) = E - H_{\rm N.R.}, \tag{A30}$$

$$\frac{d\boldsymbol{r}_i}{d\tau} = \frac{\partial H_{\rm N.R.}}{\partial \boldsymbol{p}_i} \approx \frac{\boldsymbol{p}_i}{m_i} + \sum_{j=1}^N \frac{\partial V_j}{\partial \boldsymbol{p}_i}, \tag{A31}$$

$$\frac{d\boldsymbol{p}_i}{d\tau} = -\frac{\partial H_{\rm N.R.}}{\partial \boldsymbol{r}_i} \approx -\sum_{j=1}^N \frac{\partial V_j}{\partial \boldsymbol{r}_i}. \tag{A32}$$

[1] W. Scheid, H. Müller, and W. Greiner, Phys. Rev. Lett. **32**, 741 (1974).
[2] J. Kapusta and D. Strottman, Phys. Lett. **B106**, 33 (1981).
[3] H. Stöcker, L. P. Csernai, G. Graebner, G. Buchwald, H. Kruse, R. Y. Cusson, J. A. Maruhn, and W. Greiner, Phys. Rev. C **25**, 1873 (1982).
[4] H. A. Gustafsson *et al*., Phys. Rev. Lett. **52**, 1590 (1984).
[5] G. F. Bertsch and S. Das Gupta, Phys. Rep. **160**, 189 (1988).
[6] C. Gale, G. Bertsch, and S. Das Gupta, Phys. Rev. C **35**, 1666 (1987).
[7] G. M. Welke, M. Prakash, T. T. S. Kuo, S. Das Gupta, and C. Gale, Phys. Rev. C **38**, 2101 (1988).
[8] L. P. Csernai, G. Fai, C. Gale, and E. Osnes, Phys. Rev. C **46**, 736 (1992).
[9] S. Soff, S. A. Bass, C. Hartnack, H. Stöcker, and W. Greiner, Phys. Rev. C **51**, 3320 (1995).
[10] J. Chance *et al*. (EOS Collaboration), Phys. Rev. Lett. **78**, 2535 (1997).
[11] J. C. Kintner *et al*., Phys. Rev. Lett. **78**, 4165 (1997).
[12] K. G. R. Doss *et al*., Phys. Rev. Lett. **57**, 302 (1986).
[13] N. Bastid *et al*. (FOPI Collaboration), Nucl. Phys. **A622**, 573 (1997).
[14] A. Andronic *et al*. (FOPI Collaboration), Phys. Rev. C **67**, 034907 (2003).
[15] G. Stoicea *et al*. (FOPI Collaboration) and P. Danielewicz, Phys. Rev. Lett. **92**, 072303 (2004).
[16] R. Pak, O. Bjarki, S. A. Hannuschke, R. A. Lacey, J. Lauret, W. J. Llope, A. Nadasen, N. T. B. Stone, A. M. Vander Molen, and G. D. Westfall, Phys. Rev. C **54**, 2457 (1996).
[17] P. Chung *et al*. (E895 Collaboration) and P. Danielewicz, Phys. Rev. C **66**, 021901(R) (2002).
[18] J. Barrette *et al*. (E877 Collaboration), Phys. Rev. C **55**, 1420 (1997); **56**, 3254 (1997).
[19] C. Pinkenburg *et al*. (E895 Collaboration), Phys. Rev. Lett. **83**, 1295 (1999).
[20] H. Liu *et al*. (E895 Collaboration), Phys. Rev. Lett. **84**, 5488 (2000).
[21] J. L. Klay *et al*. (E895 Collaboration), Phys. Rev. Lett. **88**, 102301 (2002).

[22] H. Appelshäuser *et al*. (NA49 Collaboration), Phys. Rev. Lett. **80**, 4136 (1998).
[23] H. Appelshäuser *et al*. (NA49 Collaboration), Phys. Rev. Lett. **82**, 2471 (1999).
[24] C. Alt *et al*. (NA49 Collaboration), Phys. Rev. C **68**, 034903 (2003).
[25] P. K. Sahu, W. Cassing, U. Mosel, and A. Ohnishi, Nucl. Phys. **A672**, 376 (2000).
[26] P. Danielewicz, Roy A. Lacey, P.-B. Gossiaux, C. Pinkenburg, P. Chung, J. M. Alexander, and R. L. McGrath, Phys. Rev. Lett. **81**, 2438 (1998).
[27] P. Danielewicz, Nucl. Phys. **A673**, 375 (2000).
[28] P. Danielewicz, R. Lacey, and W. G. Lynch, Science **298**, 1592 (2002).
[29] R. J. M. Snellings, H. Sorge, S. A. Voloshin, F. Q. Wang, and N. Xu, Phys. Rev. Lett. **84**, 2803 (2000).
[30] D. Persram and C. Gale, Phys. Rev. C **65**, 064611 (2002).
[31] A. B. Larionov, W. Cassing, C. Greiner, and U. Mosel, Phys. Rev. C **62**, 064611 (2000).
[32] T. Maruyama, W. Cassing, U. Mosel, S. Teis, and K. Weber, Nucl. Phys. **A573**, 653 (1994).
[33] P. K. Sahu and W. Cassing, Nucl. Phys. **A712**, 357 (2002).
[34] H. Stöcker, E. L. Bratkovskaya, M. Bleicher, S. Soff, and X. Zhu, J. Phys. G **31**, S929 (2005).
[35] See, for example, K. Redlich, F. Karsch, and A. Tawfik, J. Phys. G **30**, S1271 (2004) [arXiv:nucl-th/0404009]; F. Karsch, Prog. Theor. Phys. Suppl. **153**, 106 (2004) [arXiv:hep-lat/0401031]; C. R. Allton, M. Döring, S. Ejiri, S. J. Hands, O. Kaczmarek, F. Karsch, E. Laermann, and K. Redlich, Phys. Rev. D **71**, 054508 (2005) [arXiv:hep-lat/0501030], and references therein.
[36] See, for example, Nucl. Phys. **A698** (2002), and references therein.
[37] C. Adler *et al*. (STAR Collaboration), Phys. Rev. C **66**, 034904 (2002); B. B. Back *et al*. (PHOBOS Collaboration), Phys. Rev. Lett. **89**, 222301 (2002); S. S. Adler *et al*. (PHENIX Collaboration), *ibid*. **91**, 182301 (2003); J. Adams *et al*. (STAR Collaboration), *ibid*. **92**, 062301 (2004).
[38] S. Hama, B. C. Clark, E. D. Cooper, H. S. Sherif, and R. L. Mercer, Phys. Rev. C **41**, 2737 (1990).
[39] H. Sorge, H. Stöcker, and W. Greiner, Ann. Phys. **192**, 266 (1989).
[40] H. Sorge, Phys. Rev. C **52**, 3291 (1995).
[41] H. Sorge, Phys. Lett. **B402**, 251 (1997); Phys. Rev. Lett. **82**, 2048 (1999).
[42] T. Maruyama *et al*., Nucl. Phys. **A534**, 720 (1991).
[43] T. Maruyama *et al*., Prog. Theor. Phys. **96**, 263 (1996).
[44] Y. Pang, T. J. Schlagel, and S. H. Kahana, Nucl. Phys. **A544**, 435c (1992).
[45] B. A. Li and C. M. Ko, Phys. Rev. C **52**, 2037 (1995).
[46] W. Ehehalt and W. Cassing, Nucl. Phys. **A602**, 449 (1996).
[47] L. A. Winckelmann *et al*., Nucl. Phys. **A610**, 116c (1996).
[48] S. A. Bass *et al*., Prog. Part. Nucl. Phys. **41**, 255 (1998).
[49] Y. Nara, N. Otuka, A. Ohnishi, K. Niita, and S. Chiba, Phys. Rev. C **61**, 024901 (2000).
[50] P. F. Kolb, P. Huovinen, U. W. Heinz, and H. Heiselberg, Phys. Lett. **B500**, 232 (2001); P. Huovinen, P. F. Kolb, U. W. Heinz, P. V. Ruuskanen, and S. A. Voloshin, *ibid*. **B503**, 58 (2001); P. F. Kolb, U. W. Heinz, P. Huovinen, K. J. Eskola, and K. Tuominen, Nucl. Phys. **A696**, 197 (2001); P. Huovinen, arXiv:nucl-th/0505036; T. Hirano, Phys. Rev. C **65**, 011901(R) (2001).
[51] T. Hirano and M. Gyulassy, arXiv:nucl-th/0506049.
[52] X.-N. Wang and M. Gyulassy, Phys. Rev. D **44**, 3501 (1991).
[53] T. Sjöstrand *et al*., Comput. Phys. Commun. **135**, 238 (2001).
[54] J. Aichelin, A. Rosenhauer, G. Peilert, H. Stoecker, and W. Greiner, Phys. Rev. Lett. **58**, 1926 (1987).
[55] T. Maruyama, K. Niita, K. Oyamatsu, T. Maruyama, S. Chiba, and A. Iwamoto, Phys. Rev. C **57**, 655 (1998).
[56] J. Aichelin and H. Stöcker, Phys. Lett. **B176**, 14 (1986).
[57] J.-Y. Ollitrault, Nucl. Phys. **A638**, 195c (1998).
[58] S. Soff, S. A. Bass, M. Bleicher, H. Stöcker, and W. Greiner, arXiv:nucl-th/9903061.
[59] A. Komar, Phys. Rev. D **18**, 1881 (1978); **18**, 1887 (1978); **18**, 3617 (1978).
[60] P. A. M. Dirac, Rev. Mod. Phys. **21**, 392 (1949).
[61] Y. Hirata *et al*., Nucl. Phys. **A707**, 193 (2002); Y. Hirata, Ph.D. thesis, Hokkaido University (2000).